



Dynamic thermal-hydraulic modeling and stack flow pattern analysis for all-vanadium redox flow battery



Zhongbao Wei^a, Jiyun Zhao^{a,*}, Maria Skyllas-Kazacos^b, Binyu Xiong^a

^a EXQUISITUS, Centre for E-City, School of Electrical & Electronic Engineering, Nanyang Technological University, Singapore 639798, Singapore

^b School of Chemical Engineering, The University of New South Wales, UNSW Sydney, NSW 2052, Australia

HIGHLIGHTS

- A dynamic thermal-hydraulic model is developed for different stack flow patterns.
- The flow rate inhomogeneity and reversible entropic heat are included in the model.
- The model is benchmarked by experiments with mean relative error of 5.85%.
- The battery performance is significantly influenced by the stack flow patterns.
- The serpentine–parallel pattern is optimal to enhance the battery performance.

ARTICLE INFO

Article history:

Received 3 January 2014
Received in revised form
24 February 2014
Accepted 27 February 2014
Available online 13 March 2014

Keywords:

All-vanadium flow battery
Dynamic thermal-hydraulic model
Electrolyte temperature
Stack flow pattern design
Flow rate inhomogeneity
Pressure drop

ABSTRACT

The present study focuses on dynamic thermal-hydraulic modeling for the all-vanadium flow battery and investigations on the impact of stack flow patterns on battery performance. The inhomogeneity of flow rate distribution and reversible entropic heat are included in the thermal-hydraulic model. The electrolyte temperature in tanks is modeled with the finite element modeling (FEM) technique considering the possible non-uniform distribution of electrolyte temperature. Results show that the established model predicts electrolyte temperature accurately under various ambient temperatures and current densities. Significant temperature gradients exist in the battery system at extremely low flow rates, while the electrolyte temperature tends to be the same in different components under relatively high flow rates. Three stack flow patterns including flow without distribution channels and two cases of flow with distribution channels are compared to investigate their effects on battery performance. It is found that the flow rates are not uniformly distributed in cells especially when the stack is not well designed, while adding distribution channels alleviates the inhomogeneous phenomenon. By comparing the three flow patterns, it is found that the serpentine–parallel pattern is preferable and effectively controls the uniformity of flow rates, pressure drop and electrolyte temperature all at expected levels.

© 2014 Elsevier B.V. All rights reserved.

1. Introduction

Although fossil fuels are not a clean energy resource because of the serious pollutant emission, coal-fired energy has played a dominant role in the electrical power generation industry for a long time [1,2]. Renewable energy has been viewed as the promising substitute for coal-fired energy during the past years because it can save the limited fossil fuels while reducing pollution and greenhouse gas emissions. The intermittent nature of renewable energy, however, has posed a rigorous challenge for widespread application. Recent advances and developments in large-capacity batteries

have made it possible for renewable energy to be used in a continuous and steady way [3,4]. Among the multitude of large-capacity batteries, the all-vanadium redox flow battery (VRB) proposed by Skyllas-Kazacos and co-workers [5,6] in the University of New South Wales has been viewed as the most promising. VRBs have also been successfully commercialized in many countries for the unique advantages of elimination of cross contamination, independent capacity and output power design, tolerance to deep discharge, high energy efficiency and long life cycle [6–9].

Thermal modeling is a valuable tool that should be considered for VRB design and operation. For one reason, the electrolytes should be strictly controlled within a specific temperature range for the battery to work efficiently [10]. For instance, for typical electrolytes with 1.8–2 M vanadium sulfate in 2.5–3 M sulfuric acid,

* Corresponding author. Tel.: +65 6790 4508; fax: +65 6793 3318.
E-mail address: jyzhao@ntu.edu.sg (J. Zhao).

Nomenclature			
A	surface or cross-section area (m^2)	ΔS_r^\ominus	standard molar reaction entropy ($\text{J K}^{-1} \text{mol}^{-1}$)
a	sign factor	T	temperature (K)
c_p	specific heat of electrolyte ($\text{J kg}^{-1} \text{K}^{-1}$)	t	time (h)
c	concentration of species (mol L^{-1})	V	volume (L)
d	diameter (m)	w	width (m)
D_h	hydraulic diameter (m)	x	characteristic length (m)
d_f	mean fiber diameter of electrode (m)	z	number of moles of electrons exchanged in a reaction
E^\ominus	standard electrode potential (V)	<i>Greek symbol</i>	
F	Faraday's constant (C mol^{-1})	μ	dynamic viscosity (Pa s)
f	friction resistance coefficient	ε	porosity of graphite felt electrode
g	acceleration due to gravity (m s^{-2})	θ	thickness (m)
Gr	Grashof number	ρ	density (kg m^{-3})
ΔG^\ominus	standard molar Gibbs free reaction enthalpy (J mol^{-1})	β	volumetric thermal expansion coefficient
ΔH_r^\ominus	standard molar reaction enthalpy (J mol^{-1})	γ	activity coefficient
h	overall heat transfer coefficient ($\text{W m}^{-2} \text{K}^{-1}$)	<i>Subscript</i>	
L	length (m)	c	distribution channels
I	current (A)	com	flow combination
K_p	permeability coefficient	e	electrode
K_{ck}	Carman–Kozeny constant	ec	electrode with channels on surface
K	resistance coefficient	f	fluid
k	thermal conductivity ($\text{W m}^{-1} \text{K}^{-1}$)	i	inner surface
N	number of cells	in	inlet
Nu	Nusselt number	m	manifold channel
P	power (W)	mi	input manifold channel
p	pressure (Pa)	mo	output manifold channel
Δp	pressure drop (Pa)	o	outer surface
Pr	Prandtl number	p	pipe
Q	operating flow rate ($\text{cm}^3 \text{s}^{-1}$)	pi	pipe connecting the inlet of stack and outlet of tank
q	flow rate in cells ($\text{cm}^3 \text{s}^{-1}$)	po	pipe connecting the outlet of stack and inlet of tank
R	gas constant ($\text{J K}^{-1} \text{mol}^{-1}$)	r	rib
r	radius (m)	sep	flow separation
Ra	Rayleigh number	s	stack
Re	Reynolds number	t	tank
R_c	stack resistance during charge (Ω)	w	wall
R_d	stack resistance during discharge (Ω)	$+$	positive side
SOC	state of charge (%)	$-$	negative side

thermal precipitation of V^{5+} happens when the temperature is higher than 40°C over extended periods, while precipitation of $\text{V}^{2+}/\text{V}^{3+}$ occurs when the electrolyte temperature drops below 5°C [11]. Battery efficiency cannot be confirmed and the precipitation can even block the electrolyte channels if the temperature is left uncontrolled. Although precipitation can be minimized by lowering the vanadium ion concentration below 1.8 M, this leads to a reduced energy density that is often undesirable. For this purpose, a temperature control system is highly desirable for the high-efficiency operation of the VRB, although such a battery control system can only be established based on the accurate on-line prediction of electrolyte temperature. Furthermore, accurate temperature prediction serves as the requisite for modeling the electrical behavior of the VRB, which is vital for interfacing the battery with other power electronic devices [12]. This is because of many crucial parameters in electrical models, for example electrode potential, cell resistance and SOC determination are all related to the electrolyte temperature [13].

Though of great importance, studies on thermal modeling of VRB have been considerably limited. A two-dimensional numerical model was established by Al-Fetlawi et al. [14]. Such a numerical model was able to acquire detailed temperature distribution information in the battery and is helpful for the battery design. The

high calculation complexity and long simulating times, however, was not suitable for the dynamic control of electrolyte temperature. Tang et al. [15] first proposed a dynamic thermal model considering the energy and mass conservation. The electrolyte temperatures under both constant and varying surrounding temperature were studied. Further, the effect of self-discharge reactions was added to the model to acquire a more reasonable solution of temperature [16]. One limitation was that the reversible entropic heat [20] was simplified and incorporated into a cell resistance term. In more recent papers, Tang et al. [17,18] modeled the effect of shunt current and flow rate on battery efficiency, stack temperature, pressure losses, etc. In the earlier work, a dynamic model was built by considering the impacts of pump energy losses on the electrolyte temperature [19] but several issues were still expected to be improved. The entropic heat from chemical reaction was considered, but this heat source was simplified as enthalpy change of the electrode reaction, which reduced the accuracy of the simulations. Another essential limitation of the earlier dynamic models was that the effect of stack flow patterns was not considered and flow rate was assumed to be uniformly distributed in each cell, which actually deviated from the practical situation. Therefore, the earlier dynamic models are not adequate to be used in the practical stack design because significant non-uniform distribution of flow rates

can occur when the stack is not well designed. In addition, in the earlier models, the temperature was also considered to be uniform in each component of the system which was not always the case. All of these assumptions will affect the accuracy of the model and therefore requires further improvement.

As discussed above, stack flow pattern design is crucial, not only because it can influence the accuracy of the thermal model, but also because the stack flow pattern itself can have an impact on pressure drop, cell resistance and overall battery performance. Similar to the conclusion that different flow field designs influence the flow distribution on a specific graphite plate [21], the stack flow pattern design also determines the flow rate distribution among different cells. Considering that uniform electrolyte distribution in the whole reaction region is the prerequisite of high-efficiency operation of the battery, stack flow pattern is an important parameter for investigation and optimization.

Many stack flow patterns have been proposed and tested to improve the efficiency of VRB during the past years. Apart from the conventional flow-through pattern, other stack flow patterns like the serpentine and parallel patterns proposed for use in fuel cells, have also been adapted and reported for the VRB [22–24]. Xu et al. [25] presented a three-dimensional model to compare the battery efficiencies under different stack flow patterns. The results showed that the serpentine pattern is better than the parallel and conventional flow-through pattern considering the lower over-potential. In another study [21], the flow rate distribution in different channels of the same plate was studied with different flow patterns considered. These works succeeded in revealing how the stack flow pattern design can influence battery performance but were only limited to lab-scale single cells. The effect of stack flow pattern on the whole stack with several parallel aligned cells was not investigated. Furthermore, the thermal behavior of the battery under different stack flow patterns was also ignored.

In the present study, a dynamic thermal-hydraulic model is established. The inhomogeneity of flow rate distribution and reversible entropic heat are included in the model. Finite element modeling (FEM) is applied for the tank to avoid errors caused by non-uniform temperature distribution when low flow rate and poor mixing is applied. Furthermore, the flow features in stack under three different flow patterns, including flow pattern without distribution channels, serpentine pattern and serpentine–parallel pattern, are investigated and compared. The effects of different flow patterns on flow rate distribution, pressure drop and electrolyte temperature are clarified. The present study can provide a feasible dynamic model for the battery temperature control system and can be further coupled into electrical models of the VRB. By integrating the hydraulic calculations, the model is also instructive for practical stack design to control flow rate uniformity, pressure drop and electrolyte temperature at expected level. The analysis of flow patterns also gives deep insights into the high-efficiency design and operation of VRB.

2. Pressure drop and pump power

In the VRB system, the motor driven pump provides mechanical power to overcome the pressure drop (hydraulic resistances) and sustain the electrolyte flow in the positive and negative half-cell electrolyte loops. Part of the total electrical energy input into the motor-pump system converts to the mechanical power mentioned above. The remaining part of the electrical energy input cannot be used by the system and is converted to heat that is dissipated to the surroundings. It should be noted that the pump power in the present study is defined as the mechanical power portion of the total electrical energy input. From the view of energy conservation, the continuous pump power supplied to the electrolytes is eventually

converted to heat and added to the electrolyte. The following equation can be used to evaluate the pump power:

$$P_{\text{pump}} = \Delta p \times Q \quad (1)$$

where Δp is the pressure drop in the stack and pipe circuit caused by hydraulic resistance, Q is the operating flow rate.

2.1. Pressure drop in stack

The pressure drop in the stack comes mainly from the hydraulic resistances of the flow fields in the cells and manifold channels that connect the cells.

2.1.1. Pressure drop in cells

The stack consists of several parallel aligned cells with internal flow fields. Different electrolyte flow patterns in the cells can result in distinctly different flow/ion distribution and pressure drop. In the present study, all the flows are assumed laminar considering the relatively low flow rate during normal operation of the VRB. This assumption is also confirmed in the calculation. In this paper, three different stack flow patterns are considered, including a flow pattern without distribution channels in the bipolar plate, a serpentine pattern and a serpentine–parallel pattern, as illustrated in Fig. 1.

Case 1: Flow without distribution channels

This flow pattern corresponds to the first design in Fig. 1. In this flowing pattern, the electrolyte flows directly through the porous electrode. According to the Darcy's law, the pressure drop can be described as:

$$\Delta p_e = \frac{\mu L_e Q}{K_p A_e} \quad (2)$$

where K_p is the permeability coefficient that can be calculated according to the Kozeny–Carman equation as below:

$$K_p = \frac{d_f^2 \varepsilon^3}{K_{ck}(1 - \varepsilon)^2} \quad (3)$$

where d_f is the mean fiber diameter of the electrode, ε is the porosity of graphite felt electrode, K_{ck} is the Carman–Kozeny constant for the fibrous medium.

Case 2: Flow with distribution channels

The two flow patterns correspond to the second and third ones in Fig. 1. The electrolytes flow through the designed channels while meanwhile permeating into the porous electrodes. Similarly, the pressure drop through the porous electrode can be calculated by:

$$\Delta p_{ec} = \frac{\mu L_c Q_e}{K A_{ec}} \quad (4)$$

where Q_e is the flow rate in porous electrodes of each cell, L_c is the length of distribution channel and A_{ec} is the characteristic area of electrode with distribution channel on the surface, which can be expressed by:

$$A_{ec} = (w_c + w_r)\theta_e \quad (5)$$

where w_c and w_r are respectively the widths of distribution channel and rib, θ_e the thickness of the porous electrode. The pressure drop through the distribution channels has basically two sources. One is

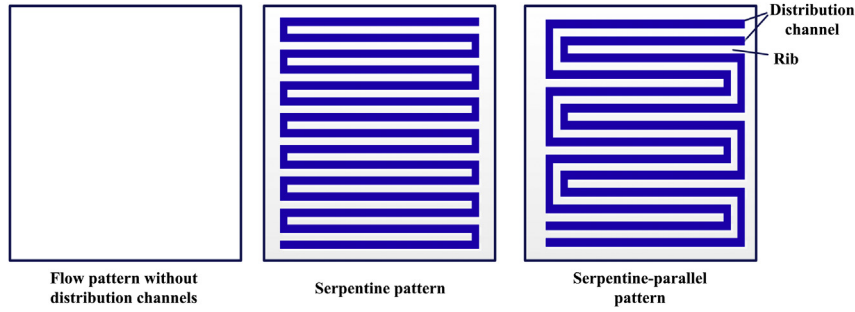


Fig. 1. Three stack flow patterns considered in the present study.

the friction pressure drop caused by the shear stress from the wall-fluid interface and within the fluid due to the viscosity of the fluid. The other source is the form pressure drop caused by sudden change of fluid direction or velocity. Taking both parts into account, the pressure drop through the channel is described as:

$$\Delta p_c = \left(f_c \frac{L_c}{D_{hc}} + K_{\text{form}} \right) \frac{\rho}{2A_c^2} Q_c^2 \quad (6)$$

where f_c is the friction resistance coefficient of the distribution channels and can be calculated by:

$$f_c = \frac{68.36 \mu A_c}{\rho D_{hc} Q_c} \quad (7)$$

where the value of 68.36 is decided by the specific geometry of channels [26]. Under steady flow state, Δp_c is equal to Δp_{ec} and the values of Q_e and Q_c can be obtained. Under steady state flow, Δp_c is equal to Δp_{ec} and the values of Q_e and Q_c can be obtained. Assuming that $Q_c = mQ$, the pressure drop in cells can finally be expressed by:

$$\Delta p_c = \left(f_c \frac{L_c}{D_{hc}} + K_f \right) \frac{\rho m^2}{2A_c^2} Q_c^2. \quad (8)$$

2.1.2. Pressure drop in the manifold channels

The resistance through the inlet and outlet manifold channels between two adjacent cells is the sum of resistance of rough pipe flow and the resistance due to the separating and combining of flow, as expressed by:

$$R_{mi} = \left(K_{\text{sep}} + \frac{f_m L_m}{D_{hm}} \right) \frac{\rho}{2A_m^2} \quad (9)$$

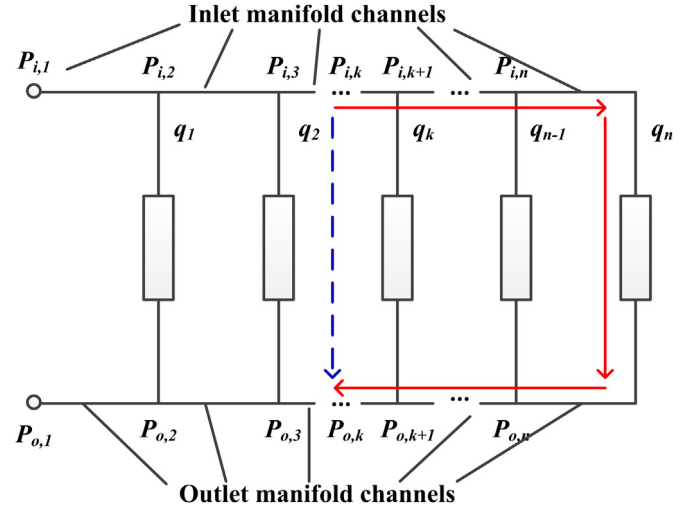


Fig. 2. Hydraulic network representing the electrolyte flow in stack.

$$R_{mo} = \left(K_{\text{com}} + \frac{f_m L_m}{D_{hm}} \right) \frac{\rho}{2A_m^2} \quad (10)$$

where K_{sep} and K_{com} are respectively the resistance coefficients of separating and combining of flow [27], L_m is the distance between two adjacent cells.

2.1.3. Pressure drop through the whole stack

Electrolyte flow in the whole stack can be treated as a hydraulic network where parallel and tandem flows happen simultaneously [28], as shown in Fig. 2. As can be seen in Fig. 2, when the electrolytes flow along the circuit represented by the solid red line (in the web version), the pressure drop can be expressed as:

$$p_{i,k} - p_{o,k} = \left(K_{\text{sep}} + \frac{f_m L_m}{D_{hm}} \right) \frac{\rho}{2A_m^2} \left[\left(\sum_{i=k}^n q_i \right)^2 + \left(\sum_{i=k+1}^n q_i \right)^2 + \dots + \left(\sum_{i=n}^n q_i \right)^2 \right] + \frac{\mu L_e}{K_p A_e} q_n + \left(K_{\text{com}} + \frac{f_m L_m}{D_{hm}} \right) \frac{\rho}{2A_m^2} \left[\left(\sum_{i=k}^n q_i \right)^2 + \left(\sum_{i=k+1}^n q_i \right)^2 + \dots + \left(\sum_{i=n}^n q_i \right)^2 \right] \quad (\text{Without distribution channels}) \quad (11)$$

$$p_{i,k} - p_{o,k} = \left(K_{\text{sep}} + \frac{f_m L_m}{D_{hm}} \right) \frac{\rho}{2A_m^2} \left[\left(\sum_{i=k}^n q_i \right)^2 + \left(\sum_{i=k+1}^n q_i \right)^2 + \dots + \left(\sum_{i=n}^n q_i \right)^2 \right] + \left(f_c \frac{L_c}{D_{hc}} + K_{\text{form}} \right) \frac{\rho}{2A_c^2} q_n^2 + \left(K_{\text{com}} + \frac{f_m L_m}{D_{hm}} \right) \frac{\rho}{2A_m^2} \left[\left(\sum_{i=k}^n q_i \right)^2 + \left(\sum_{i=k+1}^n q_i \right)^2 + \dots + \left(\sum_{i=n}^n q_i \right)^2 \right] \quad (\text{With distribution channels}) \quad (12)$$

where q_i represents the flow rate in the i -th cell. When the electrolytes flow along the path represented by the dotted blue line (in the web version), the pressure drop can be expressed as:

$$p_{i,k} - p_{o,k} = \begin{cases} \frac{\mu L_e}{K_p A_e} q_{k-1}, & \text{(Without distribution channels)} \\ \left(f_c \frac{L_c}{D_{hc}} + K_{\text{form}} \right) \frac{\rho}{2A_c^2} q_{k-1}^2, & \text{(With distribution channels)} \end{cases} \quad (13)$$

By solving Eqs. (11)–(13), the flow rate through the k -th cell can be obtained as:

$$q_{k-1} = \begin{cases} q_n + \frac{\rho K_p A_e \left(K_{\text{sep}} + K_{\text{com}} + \frac{2f_m L_m}{D_{hm}} \right)}{2\mu L_e A_m^2} \sum_{l=k}^n \left(\sum_{i=1}^n q_i \right)^2, & \text{(Without distribution channels)} \\ \left[q_n^2 + \frac{\left(K_{\text{sep}} + K_{\text{com}} + \frac{2f_m L_m}{D_{hm}} \right) A_c^2}{\left(f_c \frac{L_c}{D_{hc}} + K_{\text{form}} \right) A_m^2} \sum_{l=k}^n \left(\sum_{i=1}^n q_i \right)^2 \right]^{\frac{1}{2}}, & \text{(With distribution channels)} \end{cases} \quad (14)$$

The above equations can be solved by applying an iterative method, after which the flow rate distributions among the cells can be determined. Then the pressure drop through the whole stack can be calculated by substituting q_k into Eqs. (11) and (12).

2.2. Pressure drop in the pipe circuit

Apart from the pressure drop caused by the flow in battery stack, the pressure drop also occurs when the electrolytes flow through the pipe circuit. Similar to the flow in the distribution channels, the pressure drop in the pipe circuit can also be divided into the friction pressure drop generated along straight pipes with rough surfaces and the form loss at elbows, valves, inlet and outlet of electrolyte reservoirs. All these pressure drops can be calculated according to the discussion in Section 2.1 and will not be further repeated here.

3. Dynamic thermal-hydraulic model

The dynamic thermal-hydraulic model is established based on the energy conservation inside the stack, tanks and pipe circuits. The following assumptions are made in the present study:

- (1) The electrolyte flow is incompressible;
- (2) The positive and negative electrolytes do not change in volume during operation;
- (3) No side reactions occur when state of charge is maintained within the range 10%–90%.

3.1. Thermal behavior in stack

During discharge, the energy balance equation of the stack is expressed as below:

$$c_p \rho V_s \frac{dT_s}{dt} = Q_+ c_p \rho (T_{pi} - T_s) + Q_- c_p \rho (T_{pi} - T_s) + I^2 R_d + P_s + IT_s \frac{dE_d}{dT} \quad (15)$$

where

- T_s : the temperature of stack,
- T_{pi} : the temperature of pipe between stack inlet and tank outlet,
- R_d : the stack resistance during discharge,
- E_d : the open circuit voltage for electrode reaction during discharge,
- P_s : the pump power through the stack.

The first two terms on the right hand side of Eq. (15) are the heat accumulations due to the electrolytes exchange between pipe and stack. The third term represents the ohmic resistance heat which is positive during both charge and discharge. The fourth term is the pump power consumed in the stack, as have been discussed in Section 2. The last term represents the reversible entropic heat and can be periodically negative and positive during charge and discharge. As the entropic heat can significantly influence the thermal behavior especially for the temperature fluctuation during charge and discharge, it is included as a separate term in the present model. The entropic heat can be obtained by introducing the Nernst Equation as follows:

$$E = E^\theta + \frac{RT}{ZF} \ln \left[\left(\frac{c_{VO_2^+} c_{V^{2+}} c_{H^+}^2}{c_{VO^{2+}} c_{V^{3+}}} \right) \left(\frac{\gamma_{VO_2^+} \gamma_{V^{2+}} \gamma_{H^+}^2}{\gamma_{VO^{2+}} \gamma_{V^{3+}}} \right) \right] \quad (16)$$

where E^\ominus is the standard electrode potential for electrode reaction when the activity of each product and reactant is unity. The product term containing γ can be further set equal to 1 because the γ_i terms can be assumed to approximately cancel each other. According to the chemical thermodynamics, the following equation is established:

$$E^\ominus = \frac{\Delta G^\ominus}{zF} = -\frac{\Delta H_r^\ominus - T\Delta S_r^\ominus}{zF} \quad (17)$$

where ΔG^\ominus , ΔH_r^\ominus , and ΔS_r^\ominus are the molar Gibbs free reaction enthalpy, molar reaction enthalpy and molar reaction entropy at standard conditions respectively and the values are listed in Table 1 [29]. The value of dE/dT can be obtained by substituting (17) into (16), and the entropic heat can be expressed as:

$$IT \frac{dE}{dT} = \frac{IT}{zF} \left[\Delta S_r^\ominus + R \ln \left(\frac{c_{VO_2^+} c_{V^{2+}} c_{H^+}^2}{c_{VO^{2+}} c_{V^{3+}}} \right) \right] \quad (18)$$

The vanadium concentrations inside the cells change with the process of electrochemical reactions, resulting in different concentrations at the inlets and outlets of the cells. Therefore, the concentrations of species in Eq. (18) are referred to the average values of inlet and outlet. The input concentration is equal to the concentration in tank and can be expressed as:

$$c_{in}(t) = c_{initial} + \frac{1}{V_t} \int_0^t \frac{aI(\tau)}{F} d\tau \quad (19)$$

where V_t is the volume of tank, a is the sign factor the value of which is 1 for products while -1 for the reactants. The output concentration relates to the flow rate applied to the system and is expressed as:

$$c_{out}(t) = c_{in}(t) + \frac{aNI(t)}{FQ(t)} \quad (20)$$

Above is the description of energy balance equation during discharge. Similarly, the energy conservation during charge is described as follow:

$$c_p \rho V_s \frac{dT_s}{dt} = Q_+ c_p \rho (T_{pi} - T_s) + Q_- c_p \rho (T_{pi} - T_s) + I^2 R_c + P_s + IT_s \frac{dE_c}{dT} \quad (21)$$

where R_c represents the ohmic resistance during charge. The entropic heat can be deduced with the same method as that of the discharging process.

3.2. Thermal behavior in tanks

The temperature of the electrolytes in the tanks is determined by the heat transfer between the pipe and tank brought by flow and the heat dissipated to the surroundings. In the present study, FEM is implemented to tackle the possible non-uniformed distribution phenomenon where imperfect mixing occurs in the tanks. Considering the symmetry of both tank geometry and flow, one-dimensional FEM along the axial direction of tank is conducted to improve modeling accuracy when meanwhile maintain instantaneity. The energy balance equation reads:

Table 1

Thermodynamic data for species in redox reaction at temperature of 298.15 K.

Formula	State	ΔG_f^\ominus (kJ mol ⁻¹)	ΔH_f^\ominus (kJ mol ⁻¹)	ΔS_f^\ominus (J mol ⁻¹ K ⁻¹)
V ²⁺	aq	-218.0	-226.0	-130.0
V ³⁺	aq	-251.3	-259.0	-230.0
VO ²⁺	aq	-446.4	-486.6	-133.9
VO ₂ ⁺	aq	-587.0	-649.8	-42.3
H ⁺	aq	0	0	0
H ₂ O	aq	-237.2	-285.8	69.9

$$\begin{cases} c_p \rho V_{t,1} \frac{dT_{t,1}}{dt} = Q_+ c_p \rho (T_{po} - T_{t,1}) + h_{t,1} A_{t,1} (T_{air} - T_{t,1}) \\ c_p \rho V_{t,2} \frac{dT_{t,2}}{dt} = Q_+ c_p \rho (T_{t,1} - T_{t,2}) + h_{t,2} A_{t,2} (T_{air} - T_{t,2}) \\ \dots \\ c_p \rho V_{t,j} \frac{dT_{t,j}}{dt} = Q_+ c_p \rho (T_{t,j-1} - T_{t,j}) + h_{t,j} A_{t,j} (T_{air} - T_{t,j}) \\ \dots \\ c_p \rho V_{t,l} \frac{dT_{t,l}}{dt} = Q_+ c_p \rho (T_{t,l-1} - T_{t,l}) + h_{t,l} A_{t,l} (T_{air} - T_{t,l}) \end{cases} \quad (22)$$

where $T_{t,j}$ is the temperature of electrolytes in the j -th volume element, $V_{t,j}$ is the volume of the j -th volume element, $h_{t,j}$ and $A_{t,j}$ are respectively the overall heat transfer coefficient and superficial area of tank that encompass the j -th volume element.

3.3. Thermal behavior in pipes

Similar to the energy balance of tanks, the temperatures of electrolytes in pipes are controlled by the following equations:

$$c_p \rho V_{po} \frac{dT_{po}}{dt} = Q_+ c_p \rho (T_s - T_{po}) + h_{po} A_{po} (T_{air} - T_{po}) \quad (23)$$

$$c_p \rho V_{pi} \frac{dT_{pi}}{dt} = Q_+ c_p \rho (T_{t,l} - T_{pi}) + h_{pi} A_{pi} (T_{air} - T_{pi}) \quad (24)$$

where T_{po} denotes the temperature of pipe that connect outlet of stack and inlet of tank.

3.4. Calculation of heat dissipation

The outer surfaces of the tanks and pipes are supposed to be exposed to the natural convection environment. Also, the inner surfaces of tanks can also be treated as natural convection processes because the flow velocity in the tanks can be approximated to be low. Instead, forced convection heat transfer happens between the inner walls of the pipes and electrolytes for higher flow velocities. The convective heat transfer coefficient can be calculated by:

Table 2

Empirical coefficients of experimental correlation for different geometry.

Geometry	B	c	Condition
Vertical plate or cylinder	0.59	1/4	$10^4 \leq Gr \leq 3 \times 10^9$
Horizontal plate (high temperature upward)	0.54	1/4	$10^4 \leq Ra \leq 10^7$
Horizontal plate (high temperature upward)	0.15	1/4	$10^7 \leq Ra \leq 10^{11}$
Horizontal plate (high temperature downward)	0.27	1/4	$10^5 \leq Ra \leq 10^{10}$

$$h_{\text{conv}} = Nu \frac{k_f}{x} \quad (25)$$

where Nu is the Nusselt number, k_f the thermal conductivity of fluid, x the characteristic length. The Nusselt number for the natural convection heat transfer problem can be acquired by the following experimental correlation:

$$Nu = b(Ra)^c \quad (26)$$

where b and c are the empirical coefficients which are listed in Table 2 for different geometry [26], Ra is the Rayleigh number and can be expressed by the product of Grashof number (Gr) and Prandtl number (Pr). These two numbers can be calculated by:

$$Pr = \frac{c_{pf}\mu_f}{k_f} \quad (27)$$

$$Gr = \frac{g\rho_f^2\beta\Delta T x^3}{\mu_f^2} \quad (28)$$

where c_{pf} is the specific heat of the fluid, μ_f the dynamic viscosity of fluid, β the volumetric thermal expansion coefficient, ΔT the temperature difference between wall and fluid.

For forced convection heat transfer inside the pipes, the Nusselt number can be calculated by the Sieder–Tate equation [26]:

$$Nu = 1.86 \left(\frac{Re Pr}{L_p/d_p} \right)^{\frac{1}{3}} \left(\frac{\eta}{\eta_w} \right)^{0.14} \quad (29)$$

where Re represents the Reynolds number, η/η_w describes the influence of temperature gradient in pipes and is empirically decided as 0.95 in engineering problems.

After the convective heat transfer coefficients are obtained, the overall heat transfer coefficients can be determined by:

$$h = \begin{cases} \frac{1}{\frac{1}{h_i} + \frac{r}{k_w} \ln \frac{r+\theta_w}{r} + \frac{r}{(r+\theta_w)h_o}}, & \text{(Cylindrical wall)} \\ \frac{1}{\frac{1}{h_i} + \frac{\theta_w}{k_w} + \frac{1}{h_o}}, & \text{(Flat wall)} \end{cases} \quad (30)$$

where h_i and h_o denote the convective heat transfer coefficients of the inner and outer surfaces, respectively.

4. Results and discussion

4.1. Simulation parameters

A kilowatt class VRB system with 14 cells in the stack is simulated with the model developed above. Parameters adopted in the simulation are summarized in Table 3. The electrolytes flow directly through the porous electrode without additional distribution channels. The SOC of the battery is controlled between 10% and 90%. The modeling is conducted for 25 charging–discharging cycles. The dynamic model, characterized by a set of differential equations which can be treated as a nonlinear system, is solved in the Matlab/Simulink environment.

The model assumes that no side reactions or ion diffusion across the membrane occurs during operation and a coulomb efficiency of 100% was applied. Under this condition, the charging and

Table 3
Parameters adopted in simulation.

Parameters	Value
Number of cells	14
Dimensions of stack	0.440 m × 0.34 m × 0.2 m
Area of electrode	0.0875 m ²
Thickness of graphite felt electrode	4 × 10 ^{−3} m
Porosity of felt electrode	0.68
Fiber diameter	3 × 10 ^{−15} m
Kozeny–Carman constant	5.0
Width of distribution channels	6 × 10 ^{−3} m
Depth of distribution channels	2 × 10 ^{−3} m
Diameter of manifold channels	12 × 10 ^{−3} m
Concentrations of electrolytes	Positive: 1.5 M VOSO ₄ +3 M H ₂ SO ₄ Negative: 0.75 M V ₂ (SO ₄) ₃ + 2.25 M H ₂ SO ₄
Density of electrolytes	1400 kg m ^{−3}
Specific heat of electrolytes	3200 J kg ^{−1} K ^{−1}
Dynamic viscosity of electrolytes	4.928 × 10 ^{−3} Pa s
Diameter of pipes	1 × 10 ^{−2} m
Length of pipes	3.56 m
Volume of electrolytes in each tank	7.4 L
Dimensions of tank	0.2 m × 0.2 m × 0.4 m
Thickness of tank wall	1 × 10 ^{−2} m
Thermal conductivity of tank wall	0.16 W m ^{−1} K ^{−1}
Overall heat transfer coefficient (top wall of tank)	2.995 W m ^{−2} K ^{−1}
Overall heat transfer coefficient (bottom wall of tank)	1.703 W m ^{−2} K ^{−1}
Overall heat transfer coefficient (side wall of tank)	2.873 W m ^{−2} K ^{−1}
Overall heat transfer coefficient (pipes)	3.806 W m ^{−2} K ^{−1}
Stoichiometric flow rate for current density of 40/100 mA cm ^{−2} and SOC range of 10%–90%	33.9/84.6 cm ³ s ^{−1}
Applied flow rate	125 cm ³ s ^{−1}

discharging times are determined by the below Faraday's law of electrolysis:

$$t_c = \frac{czF \left(V_t + \frac{V_s}{2} \right)}{NI_c} \eta_{\text{SOC}} \quad (31)$$

$$t_d = \frac{czF \left(V_t + \frac{V_s}{2} \right)}{NI_d} \eta_{\text{SOC}} \quad (32)$$

where η_{SOC} represents the percent range of SOC, which is 80% for the present simulation. Although Tang et al. show that ion diffusion across the membrane can lead to considerable heat generation from the self-discharge reactions, the effect on electrolyte temperature are shown to be most significant when the pumps were turned off for several hours. In this study, the pumps are assumed to remain on during the continuous charge–discharge cycling, so the thermal effect of the self-discharge reactions can be assumed to be minimal.

4.2. Validation of model

To verify the dynamic thermal–dynamic model established in the present study, the modeling results are compared with the experimental data from another published paper [30]. Experiments are conducted under different ambient temperatures. The charging current density is maintained as 40 mA cm^{−2} while the discharging current density changes from 30 mA cm^{−2} to 100 mA cm^{−2}. The flow pattern without distribution channels was applied to the stack design. The comparison of modeled and measured electrolyte temperatures in stack under different ambient temperatures is shown in Fig. 3. As can be seen, the modeled electrolyte

temperatures correspond well with the experimental ones. The mean relative error (MRE) and root mean square error (RMSE) of modeled results are 5.85% and 0.86 °C, respectively. It can be concluded that the present dynamic-hydraulic thermal model can accurately predict the temperature of electrolytes under different ambient temperatures and different charging/discharging current densities.

4.3. Temperature responses for different system components

Under a constant ambient temperature of 25 °C, the temperature responses of different system components for the flow pattern without distribution channels are investigated in this section using the developed models. The results are shown in Fig. 4. For the stack size and electrolyte volume used in this simulation, the theoretical charging and discharging times are 0.73 and 0.29 h respectively at the current densities of 40/100 mA cm⁻². As can be seen, the temperatures of all the components increase gradually during the first several cycles, then reach to the steady state and oscillate around the respective steady-state temperature. Here the steady-state temperature is defined as the arithmetic mean temperature of the last charging/discharging cycle. It can also be observed that the temperatures of the system components all decrease during charge while increase during discharge after the steady states are reached. This phenomenon can be explained by two reasons. First, the reaction rate of V⁵⁺ reduction is kinetically faster than that of V⁴⁺ oxidation. As a result, the cell resistance during charge is smaller than that during discharge, leading to more heat generated during discharge. Second, as shown in Fig. 5, the reversible entropic heat is periodically negative during charge and positive during discharge, indicating that heat absorption happens during charge while heat generation happens during discharge.

The main heat transfer among system components is realized by the flow of the electrolytes, so different flow rates can result in different heat transfer conditions between system components. As can be seen in Fig. 4, the peak temperature of electrolytes in the stack is about 1.6 °C higher than that in the tanks at the flow rate of 5 cm³ s⁻¹. This is due to the fact that low flow rate cannot efficiently transfer heat from stack to tank, making it possible for the heat accumulated in the stack. Therefore, long time operation under low flow rate should be avoided to prevent unexpected high temperatures in stack, particularly when other operating parameters, for example high charging/discharging current densities and ambient temperatures, have already increased the system temperature. By

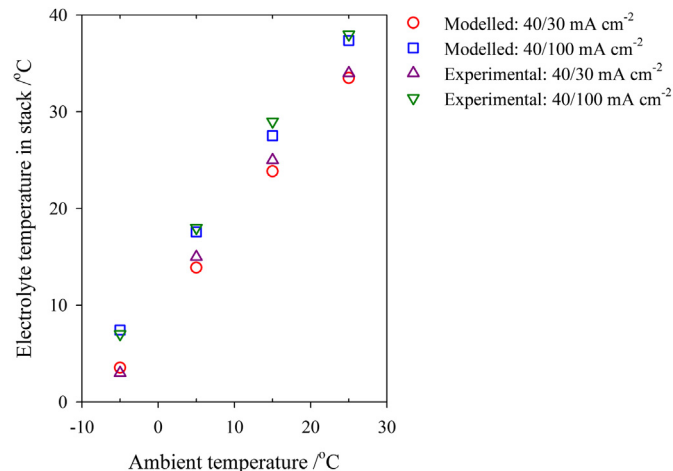


Fig. 3. Modeled and measured electrolyte temperature in stack under different ambient temperatures (unit: °C).

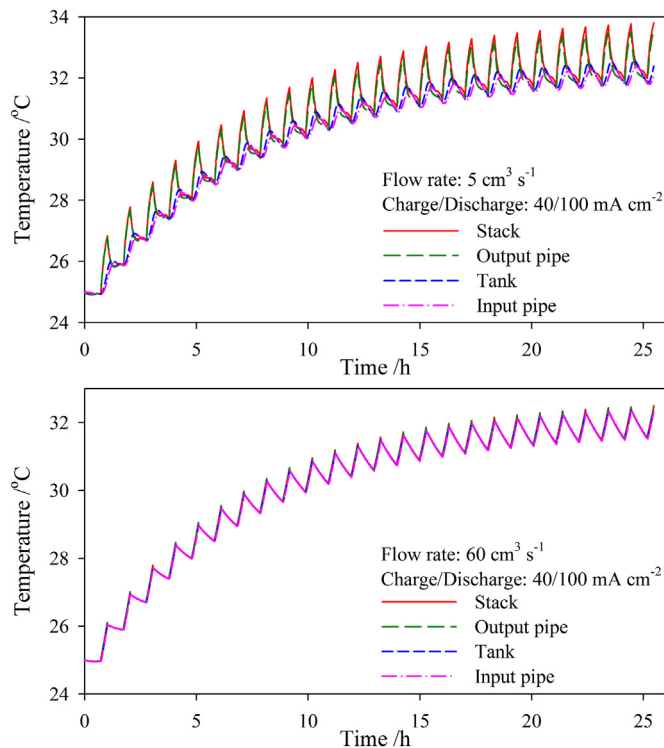


Fig. 4. Simulation results for the system temperature under two different flow rates (unit: °C).

comparison, the temperatures of system components are approximately the same at a flow rate of 60 cm³ s⁻¹, because the relatively high flow rate effectively transfers heat out of the stack and allows the temperature to distribute uniformly in the whole system.

4.4. Influence of stack flow pattern design

In this section, apart from the original flow pattern without distribution channels, two other flow patterns with distribution channels including the serpentine pattern and serpentine–parallel pattern are considered and the effects of them on battery performance are analyzed.

4.4.1. Effect of manifold channel diameter on flow rate distribution among cells

The flow resistance of the manifold channel will cause the non-uniform flow distribution among the cells. To investigate the effect of the manifold channel design and different flow patterns on the flow distribution, a sensitivity study is carried out by varying the

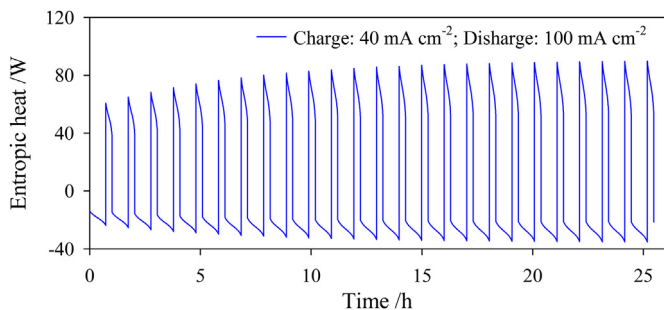


Fig. 5. Reversible entropic heat during 25 charging/discharging cycles.

manifold channel diameters for different flow patterns. The inhomogeneity coefficient (IC), defined as in Eq. (33), is adopted in order to quantitatively evaluate the inhomogeneity of flow rate distribution.

$$IC = \frac{q_{\max}}{q_{\min}} \quad (33)$$

where q_{\max} denotes the maximum cell flow rate and q_{\min} denotes the minimum cell flow rate. The flow rate of $125 \text{ cm}^3 \text{ s}^{-1}$ is adopted in the sensitivity study. The result is shown in Fig. 6.

As can be seen, the IC decreases with the increase in manifold channel diameter for all three patterns. With the same manifold channel diameter, the inhomogeneity level for the pattern without distribution channels is much higher than the two cases with distribution channels. Furthermore, the IC of pattern without distribution channels is much more sensitive to the manifold diameter. This can be explained by analyzing the hydraulic resistance in the stack. In the case without distribution channels, the relatively low flow resistance through the porous electrode is comparable to that of the manifold channels. Therefore, the change in manifold resistance caused by changing diameters will significantly influence the IC value. Instead, for the cases with distribution channels, the resistance in cell is significantly increased for the existence of long and narrow distribution channels. Compared with the cells, the resistance of manifold channels is so small that the change of it has no significant impact on the IC value. Therefore, the inhomogeneity of flow rate distribution is not much sensitive to manifold channel design.

From the above analysis, it can be seen that the non-uniform distribution of flow rate is significant if the stack is not well designed. Even if a large manifold channel diameter is applied, the inhomogeneous phenomenon still exists for all three flow patterns. Therefore, the inhomogeneous phenomenon should be considered in both thermal modeling and battery design. As shown in Table 3, a manifold channel diameter of 0.012 m is implemented in the following sections of this paper.

4.4.2. Pressure drop in stack

The pressure drop through the stack is an important parameter to be observed because it decides the pump power required to flow the electrolytes. The pressure drops in the stack with different flow patterns are shown in Fig. 7. As can be seen, the pressure drops with

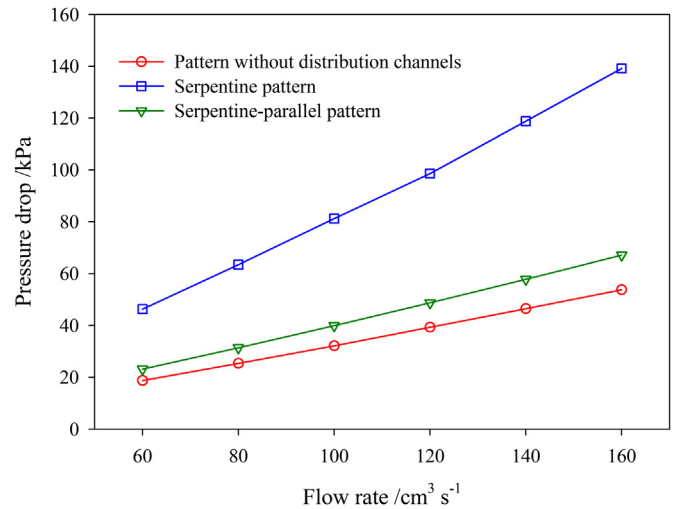


Fig. 7. Pressure drop in stack with the three flow patterns under different operating flow rates.

the three patterns all increase with increasing flow rate. The serpentine pattern yields the highest pressure drop under all the considered flow rates, which is due to the high resistance of the long and narrow serpentine channels used in the simulations. As compared, the lower resistance of the other two flow patterns helps to keep the pressure drop at a relatively low level. Though the pattern without distribution channels achieves lower pressure drop than that of serpentine–parallel pattern, the difference is not dramatic.

It should be mentioned that the present results are not totally consistent with the conclusions in other publication [25], where the author concludes that the pressure drop of flowing through porous electrode without distribution channels can be higher compared with serpentine design under low flow rate. This is because reference [25] concentrates on a lab-scale single cell with a small electrode area of $10 \text{ cm} \times 10 \text{ cm}$, so that the applied current can be considerably small and thus the battery can be operated under extremely low flow rate as 5 mL s^{-1} . In contrast, the battery in present study is kilowatt class. Though sometimes extremely low flow rate cannot be avoided, a relatively high flow rate is recommended, so a starting flow rate of $60 \text{ cm}^3 \text{ s}^{-1}$ is applied in this analysis. For comparison, the stoichiometric flow rate calculated from Faraday's Law is $84.6 \text{ cm}^3 \text{ s}^{-1}$ for a current density of 100 mA cm^{-2} at an SOC of 10%. That is the reason that the pressure drop for the flow pattern without distribution channels is always lower than that with a serpentine channel as simulated in this paper.

It is meaningful to comprehensively consider the inhomogeneity of flow distribution and pressure drop under the three patterns. Though the serpentine pattern facilitates uniform flow distribution within the cells under certain cell configurations, it may also yield the highest pressure drop. This may not be a good choice because a large pump power is demanded. On the other hand, for the flow pattern without distribution channels used in this study, the pressure drop is lower but the flow rate distribution is the most inhomogeneous, which is also undesirable. Only the serpentine–parallel pattern produces a low pressure drop while maintains uniform flow rate distribution across the cells. It should be mentioned that two parallel channels are adopted in the current study. Although the pressure drop can be further decreased by applying more parallel channels, this would be at the expense of increasing the inhomogeneity of the flow distribution. Therefore,

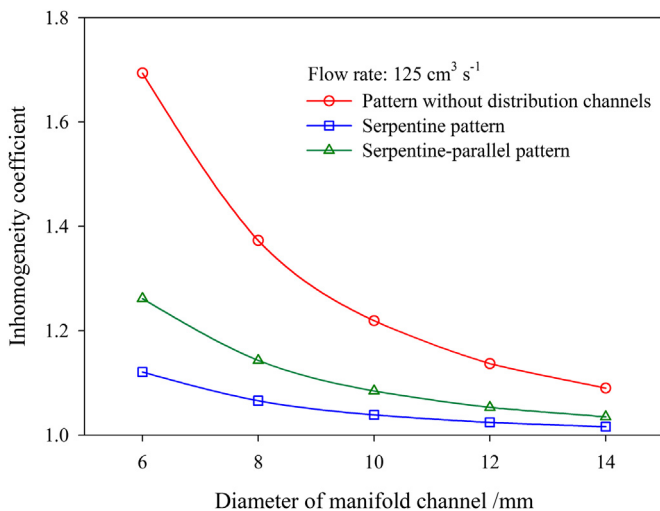


Fig. 6. Inhomogeneity coefficient of flow rate with different diameters of manifold channel.

though the serpentine–parallel pattern enhances the battery performance as a whole, designers still have to make compromises between the uniformity of flow rates and pressure drop to determine the number of parallel channels according to the practical requirement.

4.4.3. Temperature of electrolytes

In this section, the temperature of the electrolytes is discussed. As a high flow rate of $125 \text{ cm}^3 \text{ s}^{-1}$ is applied, the temperature in the whole system is uniform, as has been confirmed in Section 4.3. Under a constant ambient temperature of 25°C and charging/discharging current density of $40/100 \text{ mA cm}^{-2}$, the temperature of the electrolytes was modeled and the results under three different flow patterns are shown in Fig. 8. As can be seen, the electrolyte temperature changes by following the same trends although they are designed with different flow patterns. The steady-state temperatures are 37.3°C , 40.8°C and 37.9°C respectively for the flow pattern without distribution channels, serpentine pattern and serpentine–parallel pattern, indicating that applying distribution channels can increase the electrolyte temperature in the current case where an increased pressure drop occurs. It can also be seen in Fig. 8 that the serpentine pattern has contributed to increasing the electrolyte temperature to the thermal precipitation region, which could deteriorate the battery performance during operation.

To generalize, more simulations were conducted under different operating flow rates. Taking the case without distribution channels as reference, the temperature increases caused by adding distribution channels under different flow rates are shown in Fig. 9. As can be seen, the serpentine pattern can significantly increase the temperature of electrolytes compared with the case without distribution channels, especially when a relatively high flow rate is applied. For instance, a temperature increase of more than 5°C is observed at a flow rate of $160 \text{ cm}^3 \text{ s}^{-1}$. The significant temperature increase is caused by two reasons. First, the high pressure drop brought by the present serpentine pattern increases the pump power consumed in the stack, which generates and dissipates more heat to the electrolytes. Second, the thermal dissipation capacity of the tank is limited because a small tank was applied in the current case. With a larger tank, the phenomenon of temperature increase can be alleviated to some extent although it still exists. In contrast, the serpentine–parallel pattern also leads to temperature increase of electrolytes, but the increase is small enough to be ignored especially at a low operating flow rate. Actually, the temperature increase is also limited to within 1°C even if the battery is operated with a high flow rate. This phenomenon can be explained by the relatively low pressure drop increase caused by the serpentine–

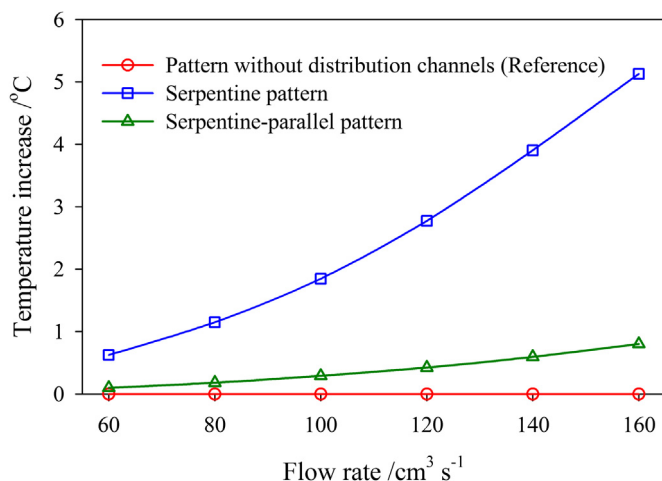


Fig. 9. Electrolyte temperature increase caused by applying distribution channels (unit: $^\circ\text{C}$).

parallel pattern used in the present study which can be seen in Fig. 7.

From the above analysis, it can be seen that the electrolyte temperature of VRB is influenced by the flow pattern design. Though the serpentine pattern facilitates the uniform distribution of flow rates in different cells, unless the channel dimensions are carefully selected, an increased pressure drop may arise leading to increased electrolyte temperature that can potentially cause the thermal precipitation of V^{5+} . By comparison, the serpentine–parallel pattern adopted in the present study can significantly improve the uniformity of the flow rate distribution while keeping the pressure drop and electrolyte temperature close to that of the pattern without distribution channels. Therefore, the choice of flow pattern should be considered seriously during VRB design to minimize the possibility of thermal precipitation.

In Section 4.4, the effect of flow pattern of stack on the thermal-hydraulic performance of battery is analyzed and the serpentine–parallel pattern is recommended by considering different factors to enhance the battery performance. In practical applications, the dimensions of channels can be further optimized for certain purpose. For instance, the pressure drop for the pattern without distribution channels is sensitive to felt compression of the electrodes. Considering a battery with highly compressed felt electrodes and thus a considerably high pressure drop across stack, if low pressure drop is the major concern, inserting distribution channels with large cross-section areas can provide an alternative path for the electrolyte flow and thus reduce the pressure drop compared with the scenario without distribution channels. As a result, the electrolyte temperature can also be reduced, but a higher inhomogeneity of flow distribution will be the byproduct. Therefore, the flow pattern and dimensions should be carefully evaluated for a specific VRB design in the practical applications.

5. Conclusions

In this study, the inhomogeneity of flow rate distribution in different cells is investigated and coupled in the dynamic thermal-hydraulic model. Finite element modeling is implemented for the tank to rule out the possible error brought by temperature non-uniformity. The reversible entropic heat is also considered as a heat source in the stack. After the dynamic model was established, three flow patterns are studied to investigate their effects on

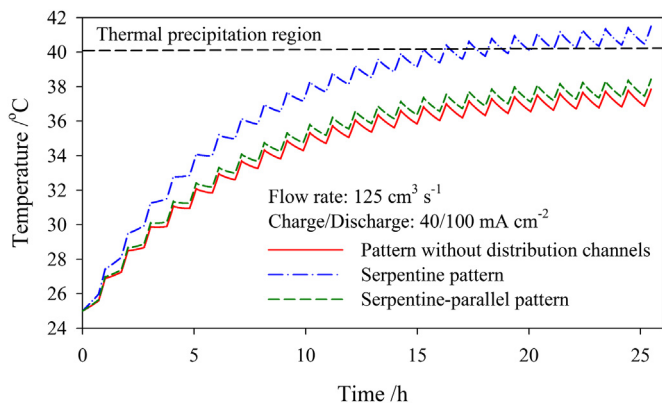


Fig. 8. Simulation result of electrolyte temperatures under three flow patterns (charge/discharge: $40/100 \text{ mA cm}^{-2}$, unit: $^\circ\text{C}$).

battery performance. The major conclusions are summarized as follows:

- (1) The established dynamic thermal-hydraulic model accurately predicts the electrolyte temperature under various ambient temperatures and charging/discharging current densities. The MRE and RMSE of modeled results are 5.85% and 0.86 °C, respectively.
- (2) The temperature distributions in the system are distinguished at different flow rate conditions. Significant temperature gradients exist in the system at an extremely low flow rate. At a relatively high flow rate, instead, the electrolyte temperature distributes uniformly in the whole system.
- (3) Non-uniform flow distribution across the cells in the stack always exists even when a large manifold channel diameter is applied, while the inhomogeneous phenomenon can be alleviated by adding distribution channels in the bipolar plate. The non-uniform flow distribution phenomenon should therefore be considered in thermal modeling and stack design of VRB.
- (4) The battery performance is significantly influenced by the design of stack flow pattern. The serpentine pattern provides the most uniform distribution of flow rates, but meanwhile significantly increases the pressure drop and the risks in causing thermal precipitation of V^{5+} with the increased electrolyte temperature. By comparison, the serpentine–parallel pattern used in the present study combines the advantages of the other two flow patterns and effectively controls the uniformity of flow rate distribution, the pressure drop and the electrolyte temperature.

References

- [1] K. Goto, K. Yogo, T. Higashii, *Appl. Energy* 111 (2013) 710–720.
- [2] Z. Wei, X. Li, L. Xu, C. Tan, *Energy Fuel* 26 (2012) 2821–2829.
- [3] A.R. Landgrebe, S.W. Donley, *Appl. Energy* 15 (1983) 127–137.
- [4] Z. Yang, J. Zhang, M.C.W. Kintner-Meyer, X. Lu, D. Choi, J.P. Lemmon, J. Liu, *Chem. Rev.* 111 (2011) 3577–3613.
- [5] E. Sum, M. Rychcik, M. Skyllas-Kazacos, *J. Power Sources* 16 (1985) 85–95.
- [6] M. Skyllas-Kazacos, M. Rychcik, R.G. Robins, A.G. Fane, M.A. Green, *J. Electrochem. Soc.* 133 (1986) 1057–1058.
- [7] M. Skyllas-Kazacos, G. Kazacos, G. Poon, H. Verseema, *Int. J. Energy Res.* 34 (2010) 182–189.
- [8] M. Skyllas-Kazacos, M.H. Chakrabarti, S.A. Hajimolana, F.S. Mjalli, M. Saleem, *J. Electrochem. Soc.* 158 (2011) R55–R79.
- [9] C. Ponce de León, A. Frías-Ferrer, J. González-García, D.A. Szánto, F.C. Walsh, *J. Power Sources* 160 (2006) 716–732.
- [10] G. Kear, A.A. Shah, F.C. Walsh, *Int. J. Energy Res.* 36 (2012) 1105–1120.
- [11] M. Kazacos, M. Cheng, M. Skyllas-Kazacos, *J. Appl. Electrochem.* 20 (1990) 463–467.
- [12] M.R. Mohamed, H. Ahmad, M.N.A. Seman, S. Razali, M.S. Najib, *J. Power Sources* 239 (2013) 284–293.
- [13] X. Feng, H.B. Gooi, S.X. Chen, in: 2012 3rd IEEE PES International Conference and Exhibition on Innovative Smart Grid Technologies (ISGT Europe), 2012, pp. 1–8.
- [14] H. Al-Fetlawi, A.A. Shah, F.C. Walsh, *Electrochim. Acta* 55 (2009) 78–89.
- [15] A. Tang, S. Ting, J. Bao, M. Skyllas-Kazacos, *J. Power Sources* 203 (2012) 165–176.
- [16] A. Tang, J. Bao, M. Skyllas-Kazacos, *J. Power Sources* 216 (2012) 489–501.
- [17] A. Tang, J. McCann, J. Bao, M. Skyllas-Kazacos, *J. Power Sources* 242 (2013) 349–356.
- [18] A. Tang, J. Bao, M. Skyllas-Kazacos, *J. Power Sources* 248 (2014) 154–162.
- [19] B. Xiong, J. Zhao, K.J. Tseng, M. Skyllas-Kazacos, T.M. Lim, Y. Zhang, *J. Power Sources* 242 (2013) 314–324.
- [20] D. Bernardi, E. Pawlikowski, J. Newman, *J. Electrochem. Soc.* 132 (1985) 5–12.
- [21] X. Bo, Q. Liang, Y. Kejian, X. Xiaofeng, *Chem. Ind. Eng. Prog.* 32 (2013) 313–319.
- [22] Q.H. Liu, G.M. Grim, A.B. Papandrew, A. Turhan, T.A. Zawodzinski, M.M. Mench, *J. Electrochem. Soc.* 159 (2012) A1246–A1252.
- [23] D.S. Aaron, Q. Liu, Z. Tang, G.M. Grim, A.B. Papandrew, A. Turhan, T.A. Zawodzinski, M.M. Mench, *J. Power Sources* 206 (2012) 450–453.
- [24] Z. Shunquan, C. Jinqing, W. Qian, W. Baoguo, *Battery Bimon.* 38 (2008) 285–287.
- [25] Q. Xu, T.S. Zhao, P.K. Leung, *Appl. Energy* 105 (2013) 47–56.
- [26] Y.A. Çengel, A.J. Ghajar, M. Kanoglu, *Heat and Mass Transfer: Fundamentals and Applications*, Yunus A. Çengel, Afshin J. Ghajar; Adapted by Mehmet Kanoglu, McGraw Hill Higher Education, c2011, New York, 2011. fourth ed. in SI units.
- [27] I.E. Idelchik, *Handbook of Hydraulic Resistance: Coefficients of Local Resistance and of Friction*, NTIS, 1960.
- [28] R.J. Boersma, N.M. Sammes, *J. Power Sources* 66 (1997) 41–45.
- [29] C. Blanc, *Modeling of a Vanadium Redox Flow Battery Electricity Storage System* (PhD thesis), 2009.
- [30] C. Sun, J. Chen, H. Zhang, Z. Yang, *Battery Bimon.* 39 (2009) 297–300.